Carbon nanomaterials with Thymol + Menthol Type V natural deep eutectic solvent: From surface properties to nano-Venturi effect through nanopores

Nuria Aguilar [a], Rocío Barros [b], Juan Antonio Tamayo-Ramos [b], Sonia Martel [b], Alfredo Bol [b,c], Mert Atilhan [d,*], Santiago Aparicio [a,b,*]

[a] Department of Chemistry, University of Burgos, 09001 Burgos, Spain
[b] International Research Centre in Critical Raw Materials-ICCRAM, University of Burgos, Plaza Misael Banuelos s/n, 09001 Burgos, Spain
[c] Department of Physics, University of Burgos, 09001 Burgos, Spain
[d] Department of Chemical and Paper Engineering, Western Michigan University, Kalamazoo, MI 49008-5462, USA

ARTICLE INFO

ABSTRACT

A theoretical study using Density Functional Theory and classical Molecular Dynamics simulations for the study of carbon nanomaterials in archetypical Menthol + Thymol Type V Natural Deep Eutectic Solvent is reported. The nanoscopic structure of the representative nanofluid is analyzed considering confinement, adsorption and solvation effects, as well as consequences on diffusion properties through nano pores. Different types of nanomaterials were considered such as fullerenes, nanotubes, graphene and nanopores. The study of nanoscopic properties allowed to analyze the response of the solvent to the presence of the nanomaterials, taking into account solvent rearrangement and confinement in nanocavities and surfaces. This response shows liquid structure and mobility consequences, with a sort of nano-Venturi effect among them. The reported results provide for the first time a characterization of this type of natural solvents as a sustainable platform for the development of carbon – nanomaterials-based technologies.

1. Introduction

Deep Eutectic Solvents (DESs) [1] are formed by the combination of two of more compounds, which upon mixing at certain mole ratios leads to a melting temperature remarkably lower than those for the individual compounds (eutectic mixture), thus enabling liquid systems at close to ambient temperature conditions. Depending on the nature of the compounds mixed for DESs formation, they may be classified from Type I to Type V [2,3,4]. Particular attention has been paid to Type III DESs formed by the combination of an hydrogen bond acceptor (HBA, frequently a quaternary ammonium salt) and an Hydrogen Bond Donor (HBD, such as organic acids, alcohols, sugars, etc.), for which the formation of strong HBA – HBD hydrogen bonding is the main reason for the melting point depletion [5,6]. For the case of Type V DES, non-ionic HBA – HBD mixtures are considered [7]. Because of the large number of HBA – HBD combinations leading to DESs forma-

tion, properties can be fine-tuned to produce DESs specifically designed for a large range of possible applications [8,9].

Depending on the nature of the compounds involved in DESs formation, they may be also classified as Natural DESs (NADESs) [10,11], which, particularly for Types III and V, are formed by HBAs and HBDs with natural origin [12]. NADES are particularly advantageous considering their low cost [13], biodegradability, non-toxicity [14], renewable origin [15], as well as showing suitable physicochemical properties [16]. NADES have been proposed for applications in a wide range of technologies including their use as green solvents [17], in the agri-food sector [18], biotechnology [19], extraction [20], or pharmaceutical applications [21].

Type V DESs are especially convenient because the absence of ionic species leads to more suitable physicochemical properties such as low viscosity [22,23] or hydrophobicity [24], allowing their scaling up to industrial applications. Therefore, the design and use of type V – NADES may enable fluids with the most suitable properties among the available DESs being applicable to a large collection of technologies. Among the possible application of general DES, their use for nanotechnologies [25] and nanomaterials development are of particular relevance in areas such as biosensors [26], metal nanomaterials [27,28], graphene production by graphite

liquid exfoliation [29], 2D-materials technologies [30], nanotubes functionalization and dispersion [31,32], nanosorbents [33] and nanofluidics [34]. The particular case of carbon-based nanomaterials is of great interest for DES / NADES applications, considering 0D (e.g. fullerenes), 1D (e.g. nanotubes [35,36]) and 2D (e.g. graphene [37,38]) nanomaterials, from the point of view of production, stabilization (dispersion) and functionalization. Taking into account the novelty and suitable physicochemical and technoeconomic properties of Type V NADES, their use for carbon-related nanotechnologies is a highly promising area, scarcely explored.

The purpose of this work is to present a study of the interaction of an archetypical example of Type V NADES and carbon nanomaterials. As representative of Type V NADES a mixture of menthol (MEN) and thymol (THY), Fig. 1, in 1: 1 mol ratio has been selected. The chosen carbon nanomaterials, Fig. 2, are: *i*) fullerenes (C60 and C540), *ii*) Single Walled Carbon Nanotubes (SWNTs, with different internal diameters), *iii*) heterojunctions (HET, formed by the combination of two different SWNTs), *iv*) cylindrical and slit pores and *v*) graphene sheets.

The general conceptual study scheme is as follows: a detailed Density Functional Theory (DFT) study of the simplest systems is done, then the study is repeated with Molecular Dynamics (MD) for validation purposes of the results of this second technique and, finally, once the confidence on these results is achieved for the proposed systems it is applied to the more complex ones. Hence, the equilibrium interaction situation properties of these materials in MEN: THY Type V NADES were studied using a theoretical approach combining Quantum Chemistry and Molecular Dynamics methods, as just explained. MD has also been used to study the diffusion of MEN: THY 1: 1 liquid from one side to the opposite one of a graphene bilayer connected with a SWNT, Fig. 2f. Computational studies have been successfully used for the nanoscopic characterization of DES / NADES considering both bulk liquid phases [9,39] as well as their interaction with nanomaterials [30,40,41,42]. These studies have provided relevant information on nano structuring, dynamics, energetics of materials, which are required for the characterization of the selected nano systems and for MEN: THY + carbon nanomaterials considered in this work. The reported results probed for the first time the possibility of using Type V NADES for carbon nanomaterials technologies, thus providing a green, sustainable and low-cost platform for materials development.

2. Methods

DFT studies on single MEN: THY 1: 1 pairs adsorbed on periodic graphene were carried out using the Quantum Espresso software (v6.5) [43]. Graphene unit cell was obtained from Materials Project Database [44] and used to build a single layer $10 \times 10 \times 1$ supercell with dimensions $a = b = 24.68$ Å, $c = 40$ Å. The dimensions of this
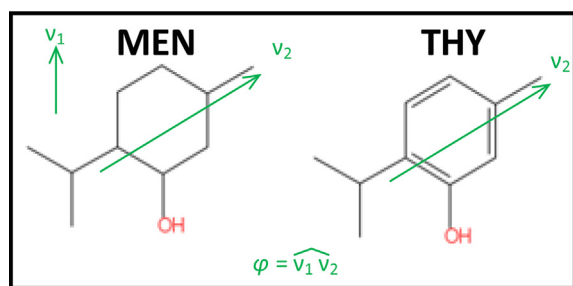
Fig. 1. Molecular structures of menthol (MEN) and thymol (THY), and directions used for orientational study (Fig. 6): v_1, is the direction perpendicular to graphene layer and v_2, is the directions defining main molecular axis of menthol and thymol.

supercell allowed the introduction of MEN: THY 1: 1 at the supercell center as well as the large vacuum layer on top, hindering the interaction of MEN: THY molecules with neighbor cells. The calculations were performed with Perdew-Burke-Ernzerhof (PBE) within the generalized gradient approximation (GGA) for exchange–correlation functional, with van der Waals interactions included with Grimme's D3 semiempirical correction [45], standard D3 correction with zero damping, i.e. DFT-D3 theoretical level is used. The combination of standard DFT methods (such as PBE) + Grimme Dispersion correction are the best compromise between quality results and computational time. Ultrasoft pseudopotentials were used for all the considered atoms [46]. Although Projector-Augmented Wave (PAW) pseudopotentials are frequently used in the literature for the study of adsorbed systems, ultrasoft pseudopotentials have been also successfully applied for the study of adsorption phenomena on graphene surfaces [47]. The Brillouin zone sampling was carried out using the Monkhorst–Pack method [48] with a $6 \times 6 \times 1$ k-grid. Calculations were done with 40 Ry for the kinetic energy cutoff. The threshold for the force minimization was 1×10^{-5} a.u. Full geometry optimizations were completed, including variable cell (with 0.5 kbar as threshold), for the previously mentioned systems: *i*) periodic graphene supercell, *ii*) MEN: THY 1: 1 dimers in vacuum, considering THY as hydrogen bond donor (P1), and MEN as hydrogen bond donor (P2), and *iii*) several configurations of these same dimers, Fig. 3, on top of the graphene layer with preferably MEN on the surface (P1a and P2a) or preferably THY on the surface (P1b and P2b). Adsorption energies, *Eads*, were calculated according to:

$$E_{ads} = E_{G+M:T} - (E_G + E_{M:T}) \tag{1}$$

Where $G + M:T$ stands for the energy of the graphene + MEN: THY 1: 1 system and G and $M:T$ for the energies of clean graphene and isolated MEN: THY 1: 1, respectively.

Classical Molecular Dynamics simulations (MD) were carried out with MDynaMix v.5.2 [49] software for the different geometries as reported in Fig. 2 for the forcefield parameterizations described in Table S1 (Supplementary Information). Initial simulation boxes were built using Packmol [50] program, with the number of MEN / THY molecules for each system adjusted to the experimental density of MEN: THY 1: 1 bulk liquid phase in absence of carbon nanomaterials ($\rho = 0.9332$ g cm^{-3} at 298.15 K, unpublished experimental result obtained in our laboratory). Ten different initial configurations were prepared for each considered system, thus leading to ten different trajectories which were combined for the analysis to improve statistical sampling and avoid possible effects derived from initial configurations. MD simulations were done setting periodic boundary conditions in the three space directions. MDs were done in the NVT ensemble at 298 K for all the systems, with the temperature being controlled using the Nosé-Hoover method [51], with 30 ps as temperature coupling time. The equations of motion were solved using the Tuckerman-Berne double time step algorithm, with long- and short-time steps of 1 and 0.1 fs. The Ewald method (1.5 nm cut-off radius) [52] was applied for handling the electrostatic interactions whereas Lennard-Jones potential was dealt with 1.5 nm cut-off distance and the Lorentz-Berthelot mixing rules for cross terms. MD simulations for each system were completed for 100 ns, for which the first 50 ns were used for equilibration purposes (assured through the analysis of systems properties) whereas the last 50 ns were devoted to production purposes and used for the analysis reported along this work. MEN: THY 1: 1 is a low viscous NADES ($\eta = 58.6$ mPa s at 298.15 K, unpublished experimental result obtained in our laboratory), thus the simulation time is long enough for a proper sampling of the considered systems properties. The visualization, analysis and postprocessing of MD trajectories was carried out using VMD [53] and TRAVIS [54].
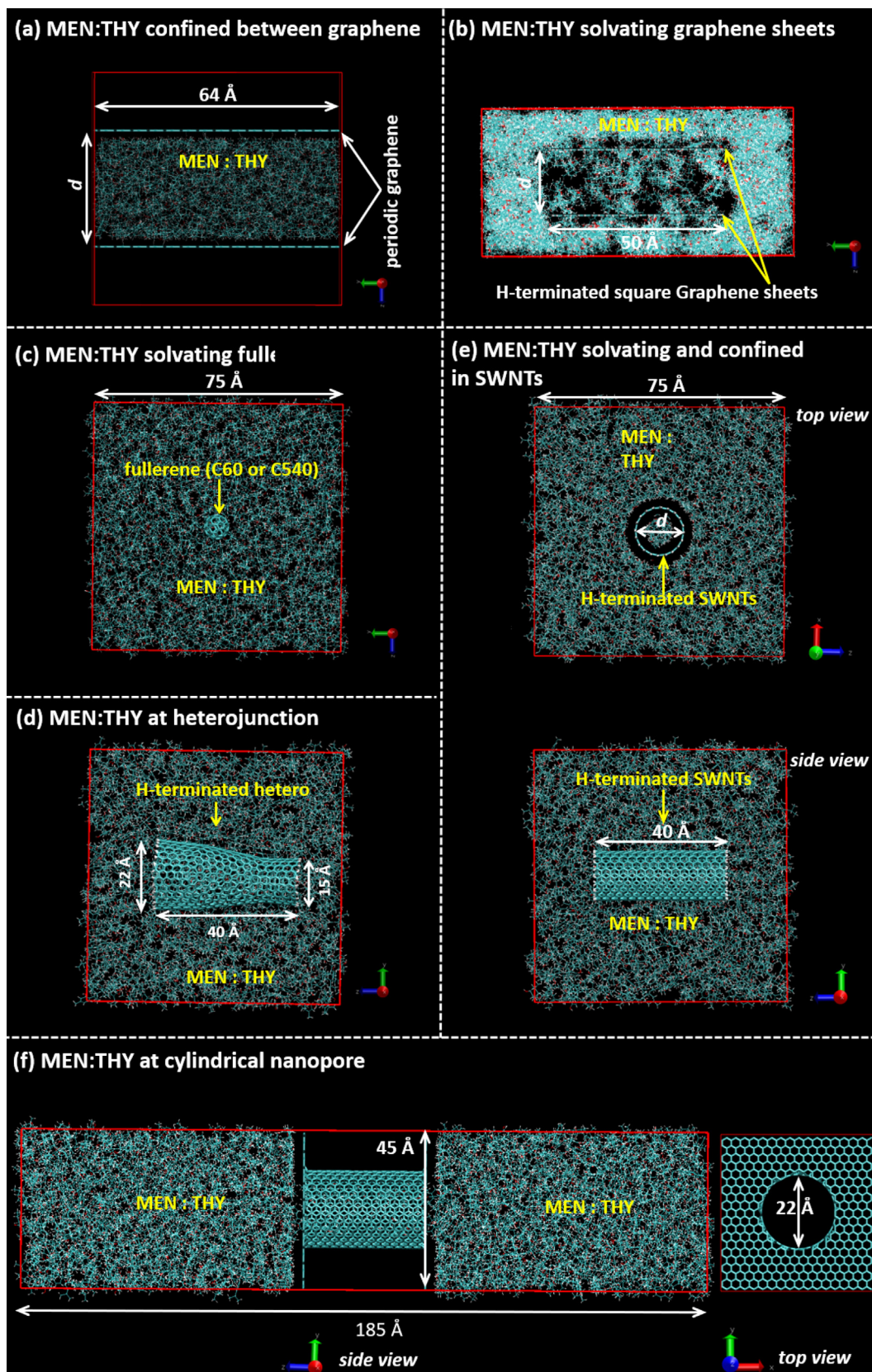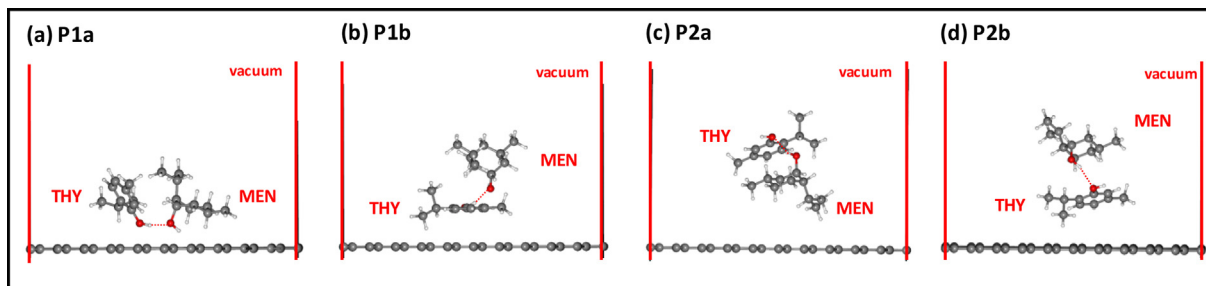
Fig. 2. Molecular structures of NADES and carbon-based nanostructures used in this work. Atom labelling indicated.
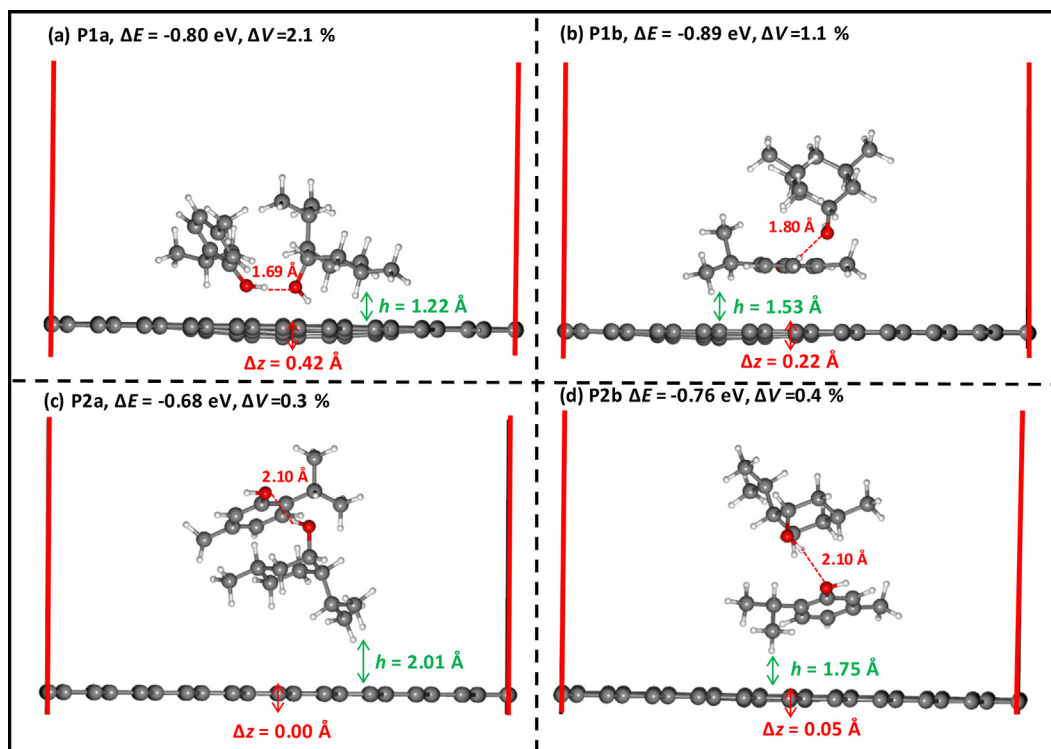
Fig. 3. Structures considered for the adsorption of MEN: THY 1: 1 dimer on periodic graphene sheet using DFT: preferably MEN on top of the graphene surface (P1a and P2a) preferably THY on top of the graphene surface (P1b and P2b). Note that the supercell used for the calculations is 40 Å high with graphene layer located at the middle.

3. Results and discussion

3.1. MEN: THY adsorbed and confined in graphene

The adsorption of MEN: THY 1: 1 isolated dimers on graphene were initially studied using DFT – D3 for the orientations and interactions reported in Fig. 3, with the main results summarized in Fig. 4. The interaction of MEN: THY dimmers with graphene surface is characterized by a strong adsorption. Dimmers with THY acting as hydrogen bond donor (P1 systems) leads to larger adsorption energies than those with MEN acting as donor. Likewise, structures with THY placed on top of the graphene surface (P1b and P2b) lead to stronger adsorption, which can be justified considering the matching between the THY and graphene aromatic rings, as can be viewed in Fig. 4. Nevertheless, adsorption energies are in the 0.69 to 0.89 eV, which confirms strong interactions for all the possible orientations. The adsorption is characterized by NADES molecules placed close to the surface (1.2 to 2.0 Å range), with globally closer distances for P1 orientations, which would justify the larger adsorption energies. A particularly interesting feature of MEN: THY adsorption stands on the disruption by expansion of the underlying graphene surface upon adsorption, which is characterized by a non-negligible relative cell expansion (one order of magnitude larger for P1 orientations). Moreover, the adsorption leads to losing graphene planarity in the region below the MEN: THY adsorbed molecules, quantified by a shifting of carbon atoms in the graphene sheet up to 0.42 Å with respect to those in regions beyond the adsorbed ones. Therefore, the adsorption generates a protrusion with an associated electronic density depletion in the graphene unperturbed plane specially for P1 mechanisms of adsorption. Fig. S1a to S1d in Supporting Information (SI) confirms graphene structure buckling and its consequences on electronic density. Moreover, the adsorption of MEN: THY on the graphene surface also disrupts the hydrogen bonding between MEN and THY molecules. The MEN: THY dimers adsorbed on the graphene surface were extracted and the energy calculated allowing the determination of the MEN – THY interaction energy (i.e. hydrogen bonding strength). The MEN – THY interaction energy calculated for opti-

Fig. 4. DFT results for the adsorption of MEN: THY 1: 1 cluster on periodic graphene surface for the different configurations and orientations considered (Fig. 3). ΔE indicates adsorption energy, ΔV indicates cell volume expansion upon MEN: THY 1: 1 adsorption, Δz indicates maximum disruption of graphene surface measured to position of undisturbed atoms, h indicates molecule – graphene distances considered atoms in molecules closer to the surface.
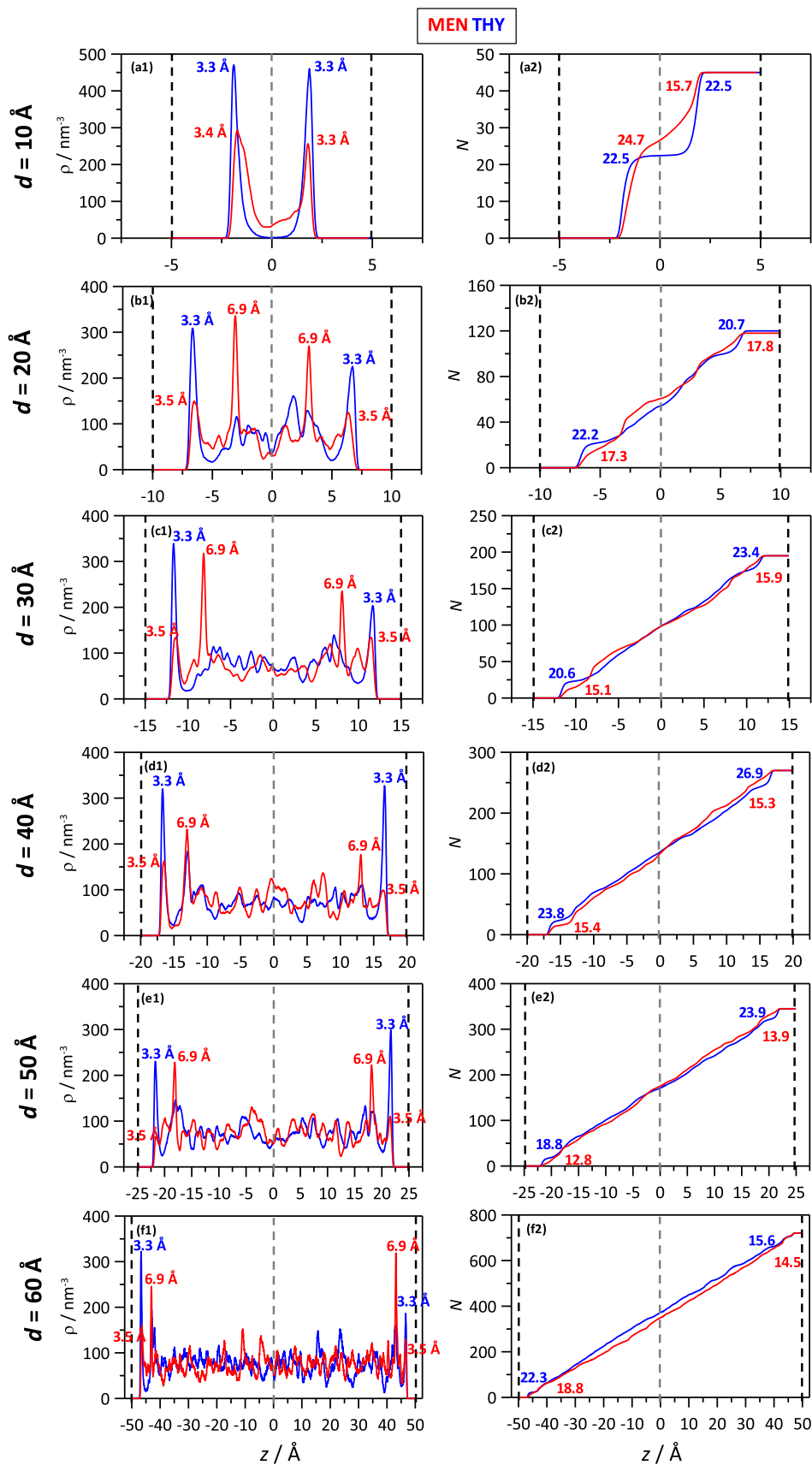
Fig. 5. (left column) Number density profiles in the direction perpendicular to the graphene surface and (right column) the corresponding integral for MEN: THY 1:1 confined between periodic graphene sheets with *d* intersheet distance (Fig. 2a). Dashed lines in panels on the left column indicate (black) the position of the graphene sheets and (gray) the center of the pore. Numeric values inside panels on the left indicate the distance to the graphene sheets corresponding to relevant peaks. Number inside panels on the right indicate the number of molecules in the layers in the first adsorbed layers (integration of the first number density peak).
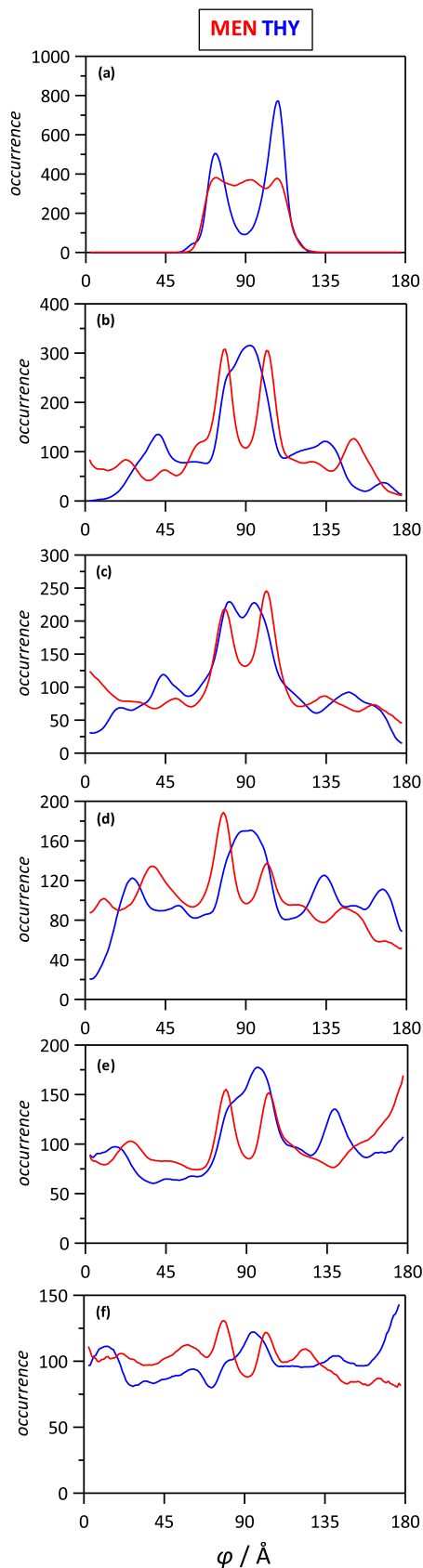
Fig. 6. Orientation of MEN or THY molecules placed in the first adsorbed layer on graphene measured by the defined φ angle for MEN: THY 1:1 (Fig. 1) confined between periodic graphene sheets with d intersheet distance (Fig. 2a).
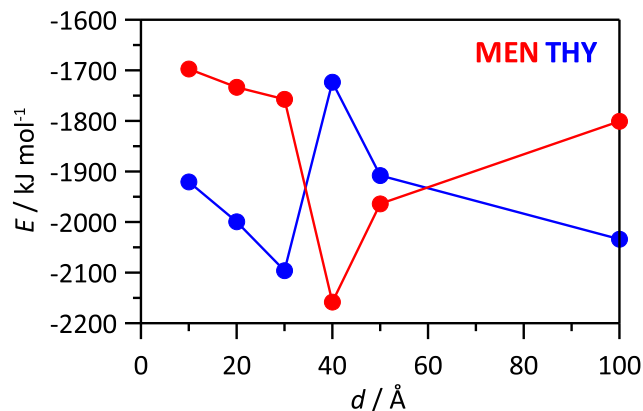
Fig. 7. Interaction energy, E, between graphene and DES component (MEN or THY) for MEN: THY 1:1 confined between periodic graphene sheets with d intersheet distance (Fig. 2a) as a function of d.
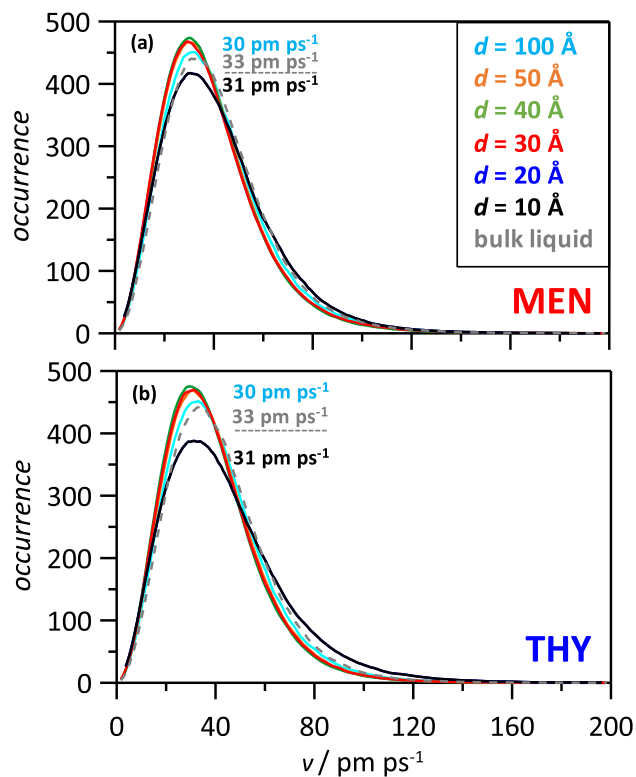
Fig. 8. Velocity, v, distribution functions for the reported molecules in MEN: THY 1:1 confined between periodic graphene sheets with d intersheet distance. Dashed gray lines show results for bulk liquid phase, i.e. in absence of confinement between graphene sheets. Values inside each panel indicate the position of the maxima. Panel a and panel b show results for MEN and THY, respectively.

mized dimers in vacuum (i.e. not adsorbed on graphene) is -0.49 and -0.31 eV, for P1 and P2 interacting positions, respectively, whereas these values decrease to -0.09 and 0.05 eV for MEN – THY dimers adsorbed on graphene. Therefore, the adsorption on graphene leads to a large disruption of MEN – THY hydrogen bonding although this interaction is maintained on the surface. It should be remarked that the dispersion contribution (Grimme – D3) is in the 4–6 % range (considering the different positions of adsorption) of the total adsorption energy, therefore, not being the main contribution to the mechanism of adsorption on the graphene surface.

The large adsorption energies, the short surface to adsorbed molecule distance as well as the disruption of the structure of the underlaying graphene surface may indicate a certain chemical sorption beyond the neat physical sorption mechanism.

The DFT confirmed the large trend of MEN: THY 1: 1 to be adsorbed on graphene surface, although considering a simplified model for isolated clusters. The behavior of the representative NADES when confined between graphene sheets (i.e. slit like nanopores) is studied using MD simulations as a function of the nanopore diameter in the 10 to 100 Å range. Number density profiles in the direction perpendicular to graphene sheets defining the nanopores, Fig. 5, confirm the development of adsorption layers in the vicinity of the surfaces. In the case of the narrower nanopore (d = 10 Å), Fig. 5a1, the density profiles show a single peak near the surface for each of the NADES components. The peaks corresponding to THY are slightly closer to the surface and are narrower and more intense than those for MEN, which agrees with DFT results in Fig. 4 showing the stronger adsorption when THY aromatic rings are placed on the graphene surface. Nevertheless, MEN adsorption is also confirmed with the wider density peaks leading to a relevant number of adsorbed molecules, Fig. 5a. The increase in nanopore size leads to the formation of a second adsorbed layer, which is placed roughly 3.6 Å above the first one. This second layer is specially defined and more intense for MEN molecules, whereas THY molecules seem to be concentrated in the first adsorbed layer. This layering leads to a first adsorbed layer richer in THY (richer in the 20–30 % range for the studied nanopore diameter) and a second layer richer in MEN, which agrees with DFT results showing preference of MEN: THY clusters with THY closer to the graphene sur-

face. The irregular molecular distribution of adsorbed molecules on graphene surface is showed in Fig. S2, in SI. A pattern of non-overlapping alternating spots corresponding to MEN and THY regions is observed. These spots correspond to MEN: THY clusters with MEN or THY on the graphene surface and with the second member of the couple of the cluster placed above the sheet corresponding to the second layer inferred from Fig. 5.

The orientation of adsorbed molecules on graphene are reported in Fig. 6 with angle definition of Fig. 1. A different behavior is observed for confinement in small nanopores (Fig. 6a, d = 1 0 Å) and the remaining wider pores (Fig. 6b to 6f). In the case of d = 10 Å nanopore, MEN molecules show an angular distribution spanning in the 60° − 120° range, which confirms that molecules are not co-planar with respect to the surface. For THY, the two peaks at 60 and 105°, indicates also a larger preference for non-planar orientations. As the nanopore diameter increases the preference of THY molecules to be arranged in a co-planar way with the graphene surface is developed, as showed by the peaks centered at 90° in Fig. 6b-6f. Complementary, for MEN two peaks at roughly 60° and 105° indicate preference to adopt skewed non-parallel orientations, which agrees with those obtained with DFT techniques, Fig. 4. Therefore, the small available space for d = 10 Å nanopore allows the development of a single adsorbed layer on each graphene surface. This steric restriction leads to a disruption of the trend of THY molecules to be adsorbed on the surface with a co-planar orientation promoting MEN – THY hydrogen bonding. But as the nanopore size increases the THY co-planar adsorption is accompanied with suitable hydrogen bonding with MEN molecules in the second adsorbed layer on top of it, thus enabling efficient THY – graphene and THY – MEN interactions. In the case of MEN molecules, the weaker interaction with graphene surface gives rise to skewed orientations upon adsorption which allows efficient MEN – THY hydrogen bonding.

The strength of MEN: THY interactions with the graphene surface upon adsorption is reported in Fig. 7. The evolution of strength
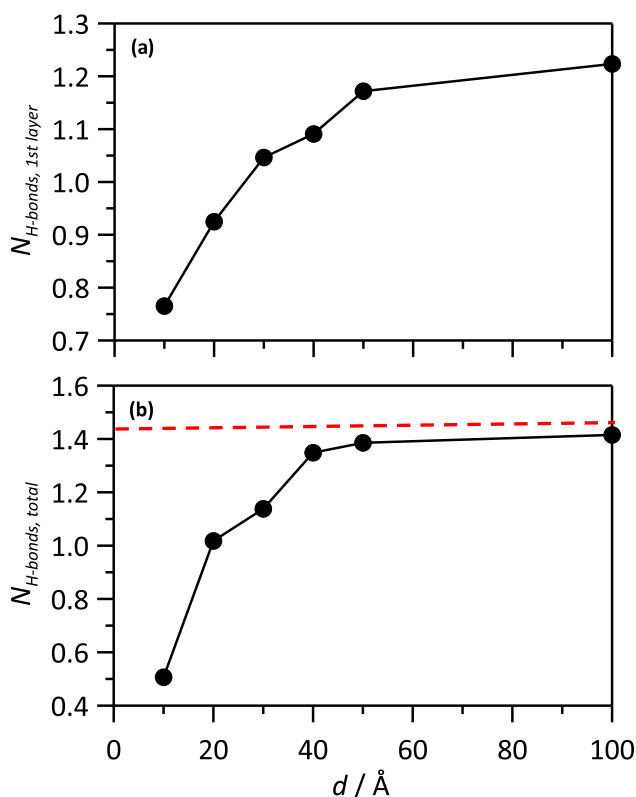
Fig. 9. Average number of hydrogen bonds per MEN molecule in MEN: THY 1:1 confined between periodic graphene sheets with d intersheet distance (Fig. 2a). Panel a shows results for molecules placed in the first adsorbed layer on graphene; panel b shows results for bulk MEN: THY 1: 1 liquid phase (i.e. in absence of graphene sheets). (For interpretation of the references to colour in this figure legend, the reader is referred to the web version of this article.)
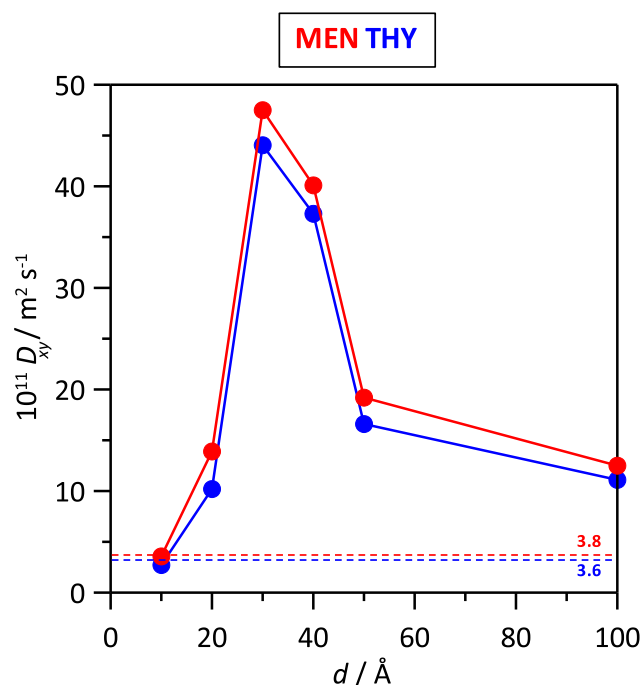
Fig. 10. Center-of-mass self-diffusion coefficient in the *xy* plane (D_{XY}), where *xy* stands for the plane containing the graphene sheets, in MEN: THY 1: 1 confined between periodic graphene sheets with d intersheet distance (Fig. 2a). Dashed lines show the values for bulk liquid phase.

interaction with nanopore size shows a complex pattern. Although for most of the nanopores, THY – graphene interaction energies are larger than MEN – graphene ones, accordingly to the trend of THY molecules to develop planar arrangements on the graphene surface, at intermediate nanopore sizes (d = 40 Å) energies for MEN are surprisingly larger than for THY. Nevertheless, results in Fig. S3 indicate that, as a rule, the larger number of THY adsorbed molecules in comparison with MEN ones corresponds to stronger interactions with the graphene surface.

The arrangement of MEN – THY molecules in the adsorbed layer of graphene is analyzed by the site – site Radial Distribution Function (RDFs) between the oxygen atoms in MEN and THY (Fig. S4a) as well as its evolution with nanopore size, i.e. graphene interlayer separation. RDF for MEN (O) – THY(O) is characterized in bulk liquid phase by a strong and narrow peak at 2.8 Å, which is maintained upon confinement for the molecules adsorbed on the first layer in direct contact with graphene, Fig. S4a. The intensity of this RDF peak rises with nanopore size. This shows the increase, with nanopore growth, of the interaction trough hydrogen bonding between MEN and THY molecules upon adsorption. Integration of the RDFs, Fig. S4b, illustrates this argument and justifies the linearity of the increase of the number of adsorbed MEN: THY dimers with the size of the nanopore, Fig. S4c. Therefore, the very effective adsorption of MEN: THY on the graphene surface is also accompanied by an efficient MEN – THY hydrogen bonding with molecules in the first adsorbed layer and those in the vicinity of molecules in direct contact with the graphene surface.

The molecular distribution of molecules confined in the nanopores is also analyzed by domain analysis [55] using Voronoi – based method, Fig. S5. Domain-count number is one both for MEN and THY, with the exception of the narrower nanopore, Fig. S5a. This is an evidence of an extended continuous network

for these species. Likewise, the domain volume and area, Fig. S5b and S5c, increase linearly with nanopore size. This shows a coupling between molecules in the first adsorbed layer and those in the regions not directly interacting with the surface. It also agrees with the RDFs reported in Fig. S4 and confirms that the adsorption on graphene is accompanied by efficient MEN – THY hydrogen bonding in the whole confined fluid. The calculated isoperimetric quotient, Fig. S5d, a measure of the sphericity of the molecular domains, decreases with increasing nanopore size. The largest values of this quotient correspond to the narrower nanopore, indicating sphericity domain loss as the nanopore size increases.

The dynamics of molecular movement was analyzed considering velocity distribution functions, Fig. 8, related with molecule size as well as with the developed intermolecular interactions. The reported results show distribution curves with the same maxima for MEN and THY, panels a and b of Fig. 8, in agreement with the view of MEN – THY system as a strongly coupled one through hydrogen bonding and thus twin displacement for both types of molecules. Likewise, the confinement has a minor effect on the molecular movement. The velocity distribution curves show more intense peaks but without changing the position of the maxima. This is a manifestation of a slight reinforcement of the movements at lower velocities because of confinement. Although this minor change produced by adsorption and confinement does not lead to a large perturbation of the global molecular movement because of the extended hydrogen bonding network. The almost negligible perturbation on the MEN – THY hydrogen bonding upon confinement is confirmed by the reported van Howe correlation functions, Fig. S6, which are equal for the case of bulk fluid and confined fluid, with only a minor change of the main peak at 2.8 Å corresponding to a slight decrease of molecular velocities as inferred from Fig. 8.
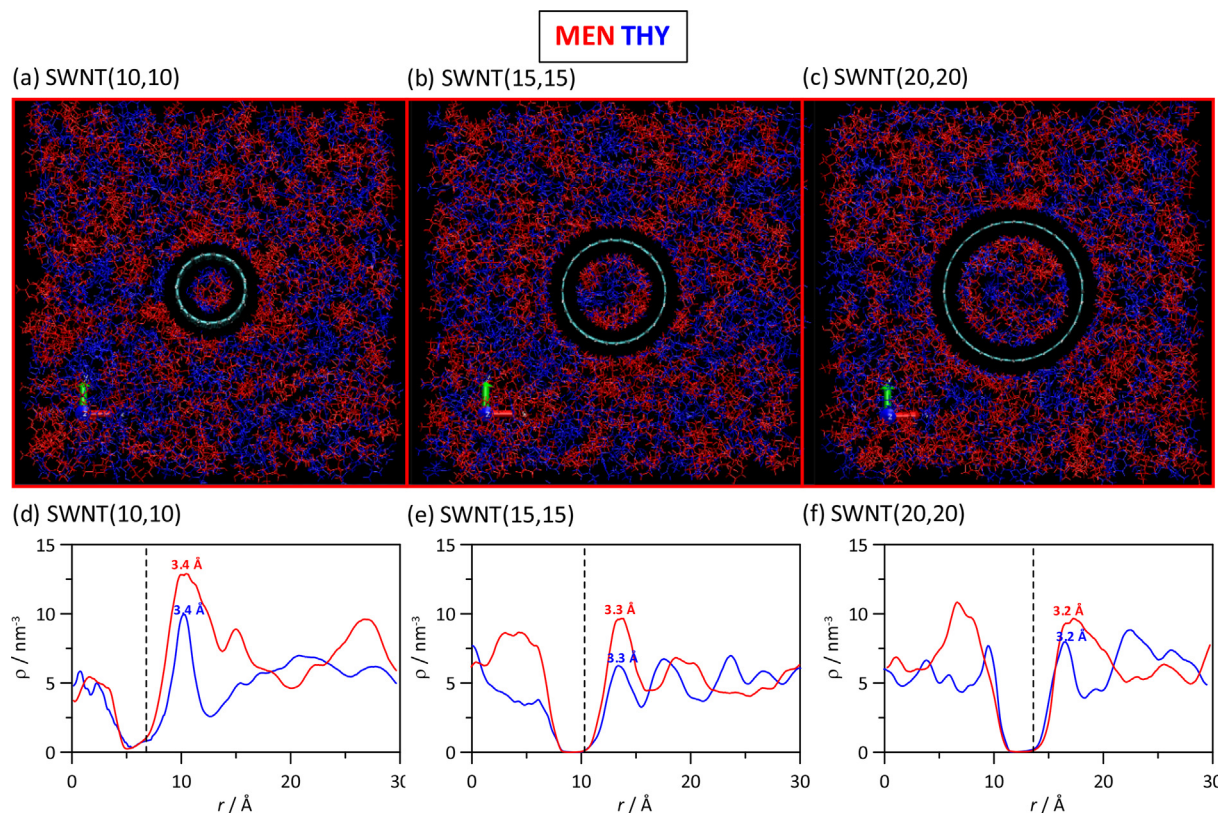
Fig. 11. (a,b,c) Snapshots and (d,e,f) number density profiles in the direction perpendicular to the SWNT long axis as a function of the distance to the SWNT longitudinal axis, r, in MEN: THY 1: 1 + SWNTs.

Although results in previous sections have probed minor changes in MEN – THY relative orientation and thus hydrogen bonding should be mostly maintained, the development of effective hydrogen bonding requires particular intermolecular orientation. We have defined a geometrical criteria considering 3.5 Å and 60° for donor – acceptor hydrogen bonding sites and quantified the number of H atoms fulfilling this criteria. Results are shown in Fig. 9. The extension of MEN – THY for those molecules placed in the first adsorbed layer on graphene, Fig. 9a, indicates that the number of hydrogen bonds per molecule decreases in a non-linear way with decreasing nanopore size. Although RDF results in Fig. S4 indicate that relative MEN – THY distribution does not change upon adsorption, the rearrangements induced by the small nanopores hinders the hydrogen bonding. This can be due to steric constraints and only when removed, because of nanopore size increase, allow the number of hydrogen bonds to approach those of unperturbed, bulk liquid, systems. The presence of nanopore not only changes the hydrogen bonding for the molecules in the adsorbed layers but the perturbative effect is extended beyond this layer disrupting the whole confined fluid, Fig. 9b. As it can be observed in this Figure only the larger nanopores (d > 50 Å) show hydrogen bonding extension similar to those in bulk liquid phase. These subtle changes in MEN – THY relative orientation are confirmed by the reported Combined Distribution Functions (CDFs) for the distance and angle relevant for hydrogen bonding, Fig. S7. Although the relevant (red) spots at 2.8 Å (in agreement with RDFs in Fig. S4) are maintained upon confinement, CDF results indicate that they are weaker for small nanopore. This indicates that the geometrical condition regarding the reported orientation angle is not fulfilled, hindering hydrogen bonding: MEN and THY molecules are arranged at suitable distances for hydrogen bonding but not at suitable orientation. This effect can be understood as the rearrangement that improves MEN/THY – graphene interactions upon adsorption, and it diminishes as the nanopore size increases approaching the CDFs bulk liquid phase. Hence, the rearrangement of molecules on the adsorbed layers does not change the MEN – THY relative distribution in terms of separation or number of neighbor molecules but hinders the fulfillment of the (angular orientation) geometrical conditions required to develop true hydrogen bonds.

It could be expected that changes in hydrogen bonding would have a reflect on molecular dynamics. We have quantified the corresponding self-diffusion coefficients, as reported in Fig. 10, and, indeed, the dynamics of MEN and THY is coupled upon confinement. This is in agreement with results of previous sections in spite of the weakening of hydrogen bonding, as it was in the bulk liquid phase. The decrease of hydrogen bonding upon confinement leads to an increase of molecular mobility in the plane parallel to graphene walls (D_{xy}) and only for the wider nanopores these values approach those of bulk liquid phase. There is also a nanopore size region in the d = 30 Å to 40 Å range with larger mobilities, which agrees with the changes in interaction energy reported in Fig. 7a: mobility echoes change in interaction energy with graphene, and thus it points to a transition from a largely confined fluid to a fluid with properties closer to the bulk liquid phase, including the evolution of hydrogen bonding.

3.2. MEN: THY solvating and confined in SWNTs / heterojunctions

The interaction between MEN: THY 1: 1 and SWNTs leads to the NADES being confined inside the nanotube (i.e. resembling with cylindrical symmetry fluid confinement in slit nanopores reported in the previous section) and also to the NADES being adsorbed in the external SWNT surface (i.e mimicking on a convex surface adsorption that on the planar one of graphene). Snapshots for the NADES distribution inside and outside the SWNTs are reported in

Fig. 11a to 11c as a function of nanotube internal diameter, confirming MEN: THY confinement and external adsorption for all the considered SWNTs. For the case of molecules inside the SWNTs, the snapshots and the density profiles reported in Fig. 11d to 11 f indicate the formation of an internal adsorbed layer on the concave internal wall of the nanotube. As the SWNT diameter increases a region of molecules placed around the center of the nanotube is also developed. For the narrower SWNT, Fig. 11a and 11d, the available space does not allow to develop a fully internal adsorbed layer as the absence of density peaks shows, and only for the wider SWNT, Fig. 11c and 11f, the properly defined adsorbed layer is developed, with THY molecules closer to the surface and MEN molecules with slight excess in internal regions. The results for SWNT(20,20) internal cavity show analogous distribution to those for graphene, Fig. 5: the increasing availability of space and the increase in nanotube diameter that leads to a decrease in the wall
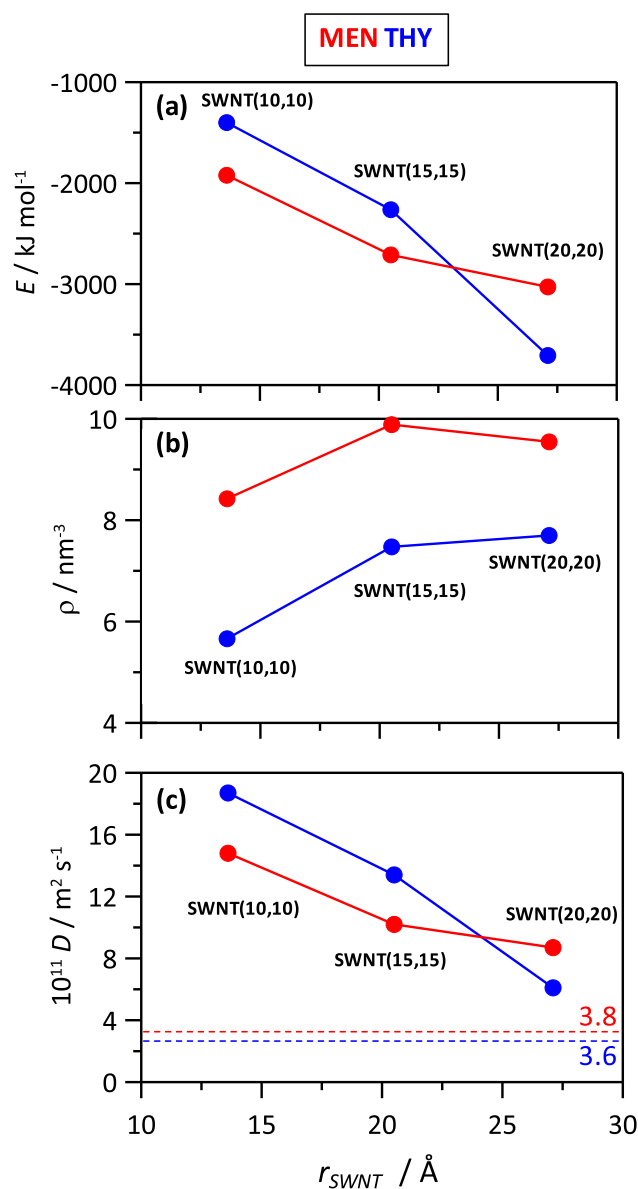
Fig. 12. (a) SWNT – MEN /THY interaction energy, E, (b) number density inside SWNTs, and (c) center-of-mass self-diffusion coefficient for molecules inside the SWNT cavity, D. Dashed lines in panel c shows D values in bulk liquid phase. All results for MEN and THY molecules, for MEN: THY 1: 1 + SWNTs as a function of SWNTs internal radius, r_{SWNT}.

curvature can be the origin of a behavior similar to graphene flat surface. In the case of NADES molecules on the outer surface of the nanotubes, a first adsorbed layer at 3.2 – 3.4 Å is inferred for all the considered SWNTs. The density peaks for THY are narrower than for MEN, which indicate an arrangement on concave surfaces similar to that in flat graphene surfaces because of the THY trend to adopt parallel arrangements also on these non-planar surfaces. Nevertheless, the interaction of MEN and THY with SWNTs, both considering confined and adsorbed molecules, is very effective as indicated by the corresponding SWNT – MEN/THY interaction energies, Fig. 12a, which are even larger than those for graphene, Fig. 7, considering interaction in concave and complex faces of the nanotubes. For narrower SWNT MEN interaction is more intense (higher interaction energy, Fig. 12a, lower density, Fig. 12b). These stronger interactions have a consequence in molecular mobility, as self-diffusion coefficients show, Fig. 12c. The main effect is an enhancement of mobility, i.e., an increase in self diffusion coefficient in comparison with bulk values. Increase in mobility as a consequence of radius reduction can be interpreted as a manifestation of Venturi effect at nanoscopic scale, nano-Venturi effect, because of the internal molecular liquid structure modification as a consequence of steric hindering. As it has been previously explained, geometrical restrictions deeply affect hydrogen bonding of this representative NADES. The second effect that can be observed in Fig. 12 a is that when the relative order of the interaction energies of THY and MEN are reversed, self-diffusion coefficients, as can be expected from Newton diffusion equation, immediately reflects this inversion, Fig. 12c, thus, approaching diffusion coefficients of MEN and THY to the in bulk liquid phase. This interaction energy increases with SWNT internal diameter as per the increase of confined molecules and the more effective interaction with the outer surface of the SWNTs, Fig. 12. The increasing confinement is confirmed in Fig. 12b, which reports the density inside the SWNTs cavity, showing a larger number of MEN molecules inside the cavity in comparison with THY. This would justify

the lower interaction energy values for THY reported in Fig. 12a, being this effect more remarkable for the narrower nanotubes.

Additional information on the molecular arrangements of confined MEN: THY is inferred from results in Fig. 13: in panel 13a isolated spots of MEN and THY (in lower concentration in Fig. 13b) are appreciated whereas as the SWNT internal diameter increases MEN domains begin to interconnect and are permeated by THY. For the wider nanopore, SWNT(20,20), the distribution is more homogeneous and both MEN and THY domains are interconnected. The quantification of MEN – THY relative distribution inside the SWNTs cavities is carried out using RDFs for MEN(O) – THY(O) pairs, Fig. 13d. The results show RDF peaks at 2.8 Å, analogous to those when confined in slit graphene nanopores, Fig. 5a, with increasing intensity as the nanotube diameter increases. Nevertheless, the calculated number of hydrogen bonds per molecule decreases upon confinement when compared with bulk liquid phase, with lower values for confinement in the narrower nanopores and increasing as the cavity size increases, Fig. 13b, thus following a parallel behavior to confinement in slit – like nanopores, Fig. 9.
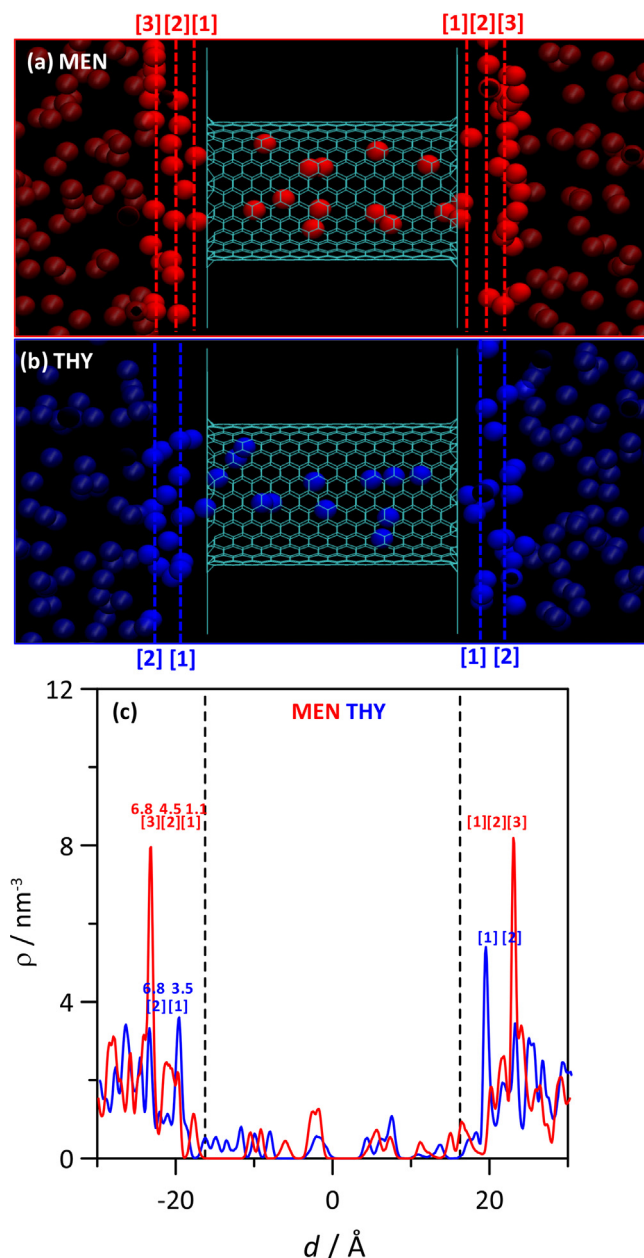
Regarding the dynamic properties upon confinement, the decrease in hydrogen bonding reported in Fig. 13e leads to an increase in molecular mobility, as it can be confirmed by self-diffusion coefficients for confined molecules 12c. In fact, they are larger than those in bulk phases, and, as this effect vanishes as the nanopore diameter increases, i.e., as the available space in the cavity enlarges, it leads to a disruption of the geometrical requirements to develop hydrogen bonding and thus determines the dynamics of the molecules inside the cavities.

Considering the prevailing role of SWNT diameter on the properties of the confined fluid, the MEN: THY distribution inside a heterojunction cavity (i.e. inside a cavity resulting from the combination of two different types of nanopores, Fig. 2d) is studied, Fig. S8. The results in Fig. S8a indicate a heterogeneous distribution inside the cavity, with heterojunction regions in the narrower side
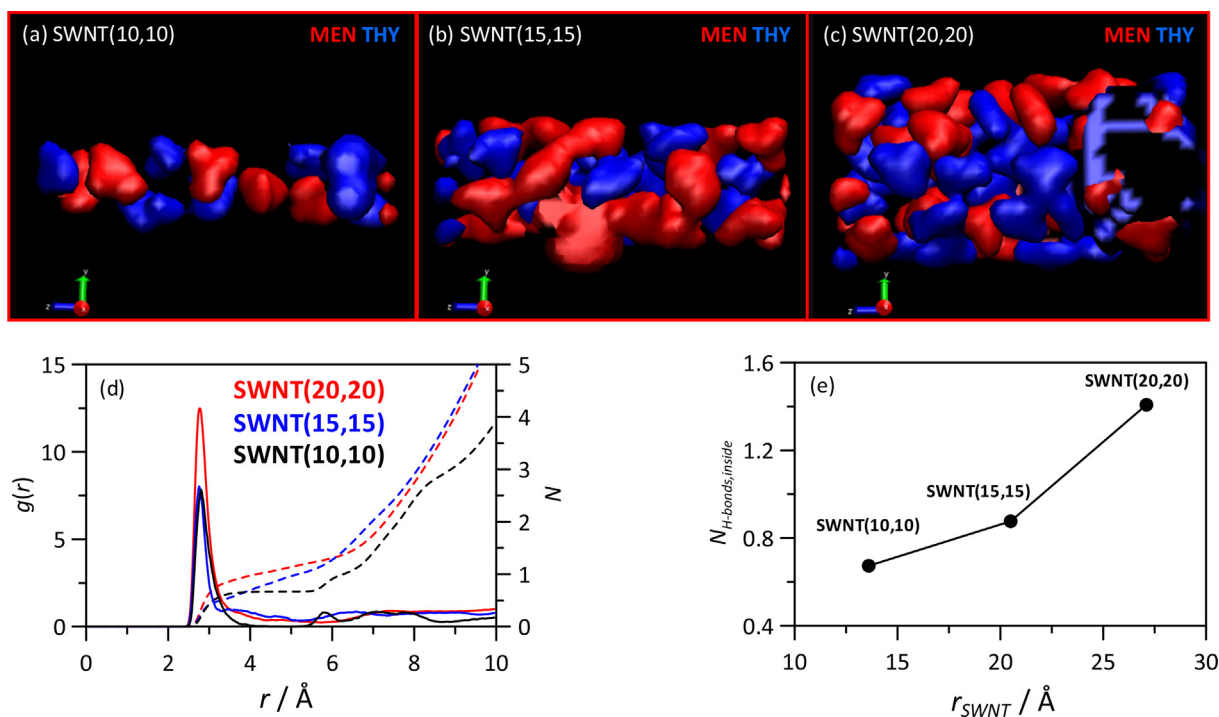
Fig. 13. Results for MEN: THY 1: 1 + SWNTs as a function of SWNTs internal radius, r_{SWNT}. Panels a to c, show distribution of molecules inside the SWNT (SWNT omitted for the sake of visibility). Panel d: Menthol (oxygen) – Thymol (oxygen) site – site radial distribution function, $g(r)$, and the corresponding integral, N, for molecules confined inside the SWNT cavity; panel e: Menthol (oxygen) – Thymol (oxygen) average number of hydrogen bonds per MEN molecule, $N_{H-bonds,inside}$, for molecules inside SWNT cavity.

being richer in THY and for the wider side showing equivalent distribution of both types of molecules. Nevertheless, the RDF for MEN (O) – THY(O) shows again the peak with maxima at 2.8 Å as for confinement in slit and cylindrical nanopores, confirming the trend of MEN – THY molecules to be associated, Fig. S8b. Moreover, the number of MEN – THY hydrogen bonds per molecule is equal to that in bulk liquid phase and analogous to the wider slit and cylindrical nanopores, Figs. 9 and 12c, and also the diffusion coefficients. Therefore, the confinement in an heterojunction leads to lower perturbative effect on MEN – THY association when the size of at least one of the combined nanotubes is wider enough to allow confinement of equivalent number of MEN and THY molecules.

The analysis of the combined behavior on flat graphene surfaces and cylindrical SWNTs cavities is performed considering the nanopore distribution reported in Fig. 2. To achieve this goal, we have studied the diffusion of MEN - THY mixture from one side of a graphene bilayer to the other through a connecting SWNT: initially a mixture of MEN – THY is placed at one side of the first graphene monolayers and the diffusion of the mixture through the SWNT to the other side of the second graphene monolayer is simulated. Results in Fig. 14 show the final equilibrium situation and how both MEN and THY molecules are arranged through the cylindrical nanopore after 100 ns simulation time. The behavior around the nanopore has two main characteristics: i) adsorption on the planar graphene surface, as indicated by the density peaks in Fig. 14c, with THY molecules closer to the surface with up to three developed consecutive layers. Also, a multilayer patter grows for MEN molecules but in outer regions, and ii) diffusion of MEN and THY along the cylindrical channel toward the other side of the nanopore arrangement. This nanofluidic diffusion pattern is confirmed in Fig. S9, where it can be inferred two diffusion layers along the nanopores: one with mole-

Fig. 14. Results for MEN: THY 1: 1 + cylindrical nanopore. Panels a and b shows snapshots around the nanopore showing the distribution of MEN / THY centers-of-mass. Panel c shows number density profiles in the direction perpendicular to the nanopore surface, with d corresponding to the distance to the nanopore central plane. Dashed lines in panel c indicate the position of the nanopore walls. Dashed lines in panels a and b, as well as labelling as in panel c indicate the position with reference to nanopore wall of the most relevant features.

Fig. 15. Selected Radial Distribution Functions, $g(r)$, and the corresponding integrals, N, for MEN: THY 1: 1 + C60 / C540. Results in panels a and b, shows fullerene (center-of-mass) – MEN/THY(center-of-mass) $g(r)$. Panel c shows Menthol (oxygen) – Thymol (oxygen) site – site radial distribution function, $g(r)$, and the corresponding integral, N, for molecules confined in the first adsorbed layer around the corresponding fullerene. Dashed lines in panels a and b indicate the position of the fullerene surface.

cules mainly adsorbed on the nanopore cylindrical wall and another one along the central axis of the nanopore.

3.3. MEN: THY solvation of fullerenes

The solvation of carbon fullerenes (C60 and C540) is first analyzed by the distribution of NADES molecules around the spherical nanoparticles, Fig. 15. In the case of the smallest fullerene, Fig. 15a, the solvation is characterized by a first layer with THY closer to the nanoparticle surface and MEN placed in slightly outer regions. Therefore, the trend to keep THY molecules closer to the surface upon adsorption is maintained in planar, graphene, and non-planar surfaces, such as nanotubes and fullerenes. For C540, Fig. 15b, the larger available surface leads to adsorption peaks closer to the surface (roughly 0.5 Å closer) and decreases the differences between the position of THY and MEN adsorption layers. Likewise, for C540 the second adsorbed layers are better defined in comparison with C60, thus inducing NADES ordering beyond the first adsorption layer. Nevertheless, these arrangements also maintain the MEN – THY interaction as inferred in Fig. 15c for MEN(O) – THY(O) RDF with the peak at 2.8 Å for both fullerenes as for the other considered surfaces in this work. Therefore, MEN: THY is also able to efficiently solvate even the smallest fullerenes upon adsorption on their surface without large disruption of the NADES self-arrangements. The interaction between the NADES and the fullerenes is quantified in Fig. 16a through the corresponding interaction energies, larger for MEN than for THY. In spite of the presence of THY molecules closer to the fullerene surfaces, MEN molecules lead to a larger second adsorbed layer in comparison with THY, Fig. 15a and 15b, which would justify the interaction energy values reported in Fig. 16a. Notwithstanding, THY molecules are closer to the surface and thus they show lower mobilities as inferred from the self-diffusion coefficients, Fig. 16b. It should be remarked that molecular diffusion of MEN and THY around fullerenes is one order of magnitude lower than for those

adsorbed-on graphene, Fig. 10, or SWNTs surfaces, Fig. 12c, and also lower than those in the bulk non-adsorbed liquid phase, see the same Figure. This can be justified considering a combination of geometrical and adsorption aspects: the extension of the available surface in fullerenes, its spherical shape and the efficient adsorption hinder the molecular motions around the solvated fullerenes. This could be a positive factor in order to consider these fluids as agents for fullerenes solubilization.

4. Conclusions

The interaction, adsorption and confinement of menthol: thymol 1: 1 type V natural deep eutectic solvent with carbon nanomaterials (graphene, nanotubes, nanopores and fullerenes) is studied using theoretical methods. The confinement of the considered fluid in slit – like graphene nanopores is characterized by strong adsorption on the nanopore walls with thymol molecules enrichment for the adsorbed layers but maintaining menthol – thymol distribution. Nevertheless, the confinement disrupts hydrogen bonding, especially for narrow nanopores, and only for pores larger than 50 Å the perturbative effect decreases and hydrogen bonding similar to the bulk fluid is restored. In the case of single walled nanotubes, the fluid penetrates into the nanotube cavity leading to confinement in cylindrical pores, and simultaneously it is adsorbed in the external wall of the nanotube. The confined fluid inside the cylindrical cavity is characterized by a faster diffusion and lower hydrogen bonding than in the case of the bulk fluid with an internal distribution characterized by molecules adsorbed on the internal convex wall and for the larger nanotubes with a region of molecules along the central axis of the nanotube. Analogous adsorption and distribution patterns are observed for heterojunctions, and the combination of graphene flat walls and cylindrical nanopores allows the diffusion of fluid molecules along the developed nanopores. This nano-structure could be used as membrane for this fluid, with diffusion patterns along the nanopore walls and the central axis of the nanopore. Moreover, very efficient solvation of fullerenes was inferred because of the suitable solvation for small and large nanoparticles upon the adsorption of the fluid on the fullerene walls, following a similar pattern to the nanotubes solvation. Therefore, the menthol: thymol fluid shows suitable properties regarding the considered 0D, 1D and 2D carbon nanomaterials, with large adsorption, solvation and confinement, which indicates that these materials could be considered for the developing of mixed carbon – deep eutectics fluids for different applications from solubilization purposes to electrochemical devices. Likewise, Venturi effect in liquids, when explained by means of continuous medium model, relies on the boundary conditions restrictions imposed to energy per unit mass distribution associated to internal tension and kinetic energy. The effect that we have found, diffusion enhancement in slit nanopores and small radius nanotubes, relies on the steric restrictions imposed to hydrogen binding that allow the decoupling of constituent liquid molecules and, as consequence, a more efficient diffusion through narrow nanostructures. This is the argument that we think allows us to properly label this as nano-Venturi effect.

Data availability

Data will be made available on request.

Declaration of Competing Interest

The authors declare that they have no known competing financial interests or personal relationships that could have appeared to influence the work reported in this paper.
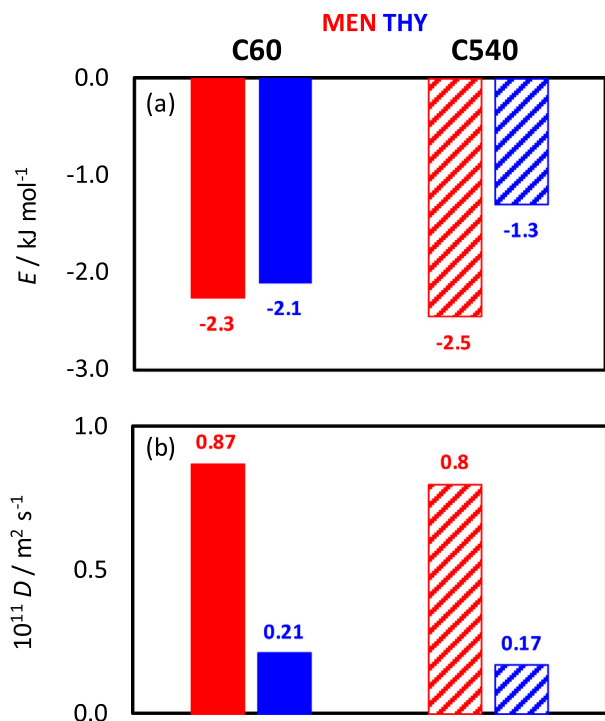
Fig. 16. (a) Interaction energy, E, between fullerenes (C60 or C50) and DES component (MEN or THY), and (b) center-of-mass self-diffusion coefficients, D, for molecules placed in the first adsorbed layer around fullerenes, in MEN: THY 1: 1 + C60 / C540. Values are reported per carbon atom in fullerene for normalization.

Acknowledgements

Appendix A. Supplementary material

Supplementary data to this article can be found online at https://doi.org/10.1016/j.molliq.2022.120637.

References

[1] A.P. Abbott, G. Capper, D.L. Davies, H.L. Munro, R.K. Rasheed, V. Tambyrajah, Preparation of novel, moisture-stable, Lewis-acidic ionic liquids containing quaternary ammonium salts with functional side chains, Chem. Comm. 19 (2001) 2010–2011.

[2] A.P. Abbott, J.C. Barron, K.S. Ryder, D. Wilson, Eutectic-based ionic liquids with metal-containing anions and cations, Chem. Eur. J. 13 (2007) 6495–6501.

[3] S. Dutta, K. Nath, Prospect of ionic liquids and deep eutectic solvents as new generation draw solution in forward osmosis process, J. Water Process Eng. 21 (2018) 163–176.

[4] N. Schaeffer, D.O. Abranches, L.P. Silva, M.A.R. Martins, P.J. Carvalho, O. Russina, A. Triolo, L. Paccou, Y. Guinet, A. Hedoux, J.A.P. Coutinho, Non-Ideality in Thymol + Menthol Type V Deep Eutectic Solvents, ACS Sustainable, Chem. Eng. 9 (5) (2021) 2203–2211.

[5] T. Zhekenov, N. Toksanbayev, Z. Kazakbayeva, D. Shaha, F.S. Mjalli, Formation of type III Deep Eutectic Solvents and effect of water on their intermolecular interactions, Fluid Phase Equilibr. 441 (2017) 43–48.

[6] D.O. Abrnaches, R.O. Martins, L.P. Silva, M.A.R. Martins, S.P. Pinho, J.A.P. Coutinho, Liquefying compounds by forming deep eutectic solvents: a case study for organic acids and alcohols, J. Phys. Chem. B 124 (2020) 4174–4184.

[7] Y. Jin, D. Jung, K. Park, J. Lee, Mixing of menthol-based hydrophobic deep eutectic solvents as a novel method to tune their properties, J. Mol. Liq. 301 (2020).

[8] T. El Achkar, H. Greige-Gerges, S. Fourmentin, Basics and properties of deep eutectic solvents: a review, Environ, Chem. Lett. 19 (4) (2021) 3397–3408.

[9] B.B. Hansen, S. Spittle, B. Chen, D. Poe, Y. Zhang, J.M. Klein, A. Horton, L. Adhikari, T. Zelovich, B.W. Doherty, B. Gurkan, E.J. Maginn, A. Ragauskas, M. Dadmun, T.A. Zawodzinski, G.A. Baker, M.E. Tuckerman, R.F. Savinell, J.R. Sangoro, Deep eutectic solvents: A review of fundamentals and applications, Chem. Rev. 121 (3) (2021) 1232–1285.

[10] Y.H. Choi, J. van Spronsen, Y. Dai, M. Verberne, F. Hollman, I.W.C.E. Arends, G.J. Witkamp, R. Verpoorte, Are Natural Deep Eutectic Solvents the missing link in understanding cellular metabolism and physiology?, Plant Phis. 156 (2011) 1701–1705.

[11] Y. Liu, B. Friesen, J.B. McAlpine, D.C. Lankin, S.N. Chen, G.F. Pauli, Natural Deep Eutectic Solvents: properties, applications, and perspectives, J. Nat. Prod. 81 (2018) 679–690.

[12] A. Paiva, R. Craveiro, I. Aroso, M. Martins, R.L. Reis, A.R.C. Duarte, Natural Deep Eutectic Solvents – Solvents for the 21st Century, ACS Sustainable Chem. Eng. 2 (5) (2014) 1063–1071.

[13] A.K. Kumar, S. Sharma, G. Dixit, E. Shah, A. Patel, G. Boczkaj, Techno-economic evaluation of a natural deep eutectic solvent-based biorefinery: Exploring different design scenarios, Biofuels Bioproducts Biorefining 14 (4) (2020) 746–763.

[14] J. Torregrosa-Crespo, X. Marset, G. Guillena, D.J. Ramón, R.M. Martinez-Espinosa, New guidelines for testing Deep eutectic solvents" toxicity and their effects on the environment and living beings, Sci. Total Environ. 704 (2020).

[15] Y. Wang, K.H. Kim, K. Jeong, N.K. Kim, C.G. Yoo, Sustainable biorefinery processes using renewable deep eutectic solvents, Curr. Opin. Green Sus. Chem. 27 (2021).

[16] A. Kovács, E.C. Neyts, I. Cornet, M. Wijnants, P. Billen, Modeling the physicochemical properties of natural deep eutectic solvents, ChemSusChem 13 (15) (2020) 3789–3804.

[17] H. Vanda, Y. Dai, E.G. Wilson, R. Verpoorte, Y.H. Choi, Green solvents from ionic liquids and deep eutectic solvents to natural deep eutectic solvents, Comptes. Ren. Chim. 21 (6) (2018) 628–638.

[18] A. Mišan, J. Nađpal, A. Stupar, M. Pojić, A. Mandić, R. Verpoorte, Y.H. Choi, The perspectives of natural deep eutectic solvents in agri-food sector, Critical Rev. Fodd Sci. Nut. 60 (15) (2020) 2564–2592.

[19] Z. Yang, Natural Deep Eutectic Solvents and Their Applications in Biotechnology. In: Itoh T., Koo YM. (eds) Application of Ionic Liquids in Biotechnology. Advances in Biochemical Engineering/Biotechnology, vol 168. Springer, Cham. https://doi.org/10.1007/10_2018_67.

[20] Y. Dai, K.H. Row, Application of Natural Deep Eutectic Solvents in the extraction of quercetin from vegetables, Molecules 24 (2019) 2300.

[21] T. Jelinski, M. Przybylek, P. Cysewski, Natural Deep Eutectic Solvents as agents for improving solubility, stability and delivery of curcumin, Pharm. Res. 36 (2019) 116.

[22] B.D. Ribeiro, C. Florindo, L.C. Iff, M.A.Z. Coelho, I.M. Marrucho, Menthol-based eutectic mixtures: hydrophobic low viscosity solvents, ACS Sustainable Chem. Eng. 3 (10) (2015) 2469–2477.

[23] D.J.G.P. van Osch, C.H.J.T. Dietz, J. van Spronsen, M.C. Kroon, F. Gallucci, M. van Sint Annaland, R. Tuinier, A search for natural hydrophobic deep eutectic solvents based on natural components, ACS Sustainable Chem. Eng. 7 (3) (2019) 2933–2942.

[24] U.S.L. Abbas, Q. Qiao, M.T. Nguyen, J. Shi, Q. Shao, Structure and hydrogen bonds of hydrophobic deep eutectic solvent-aqueous liquid–liquid interfaces, AIChE J. 67 (2021) e17427.

[25] A. Abo-Hamad, M. Hayyan, M.A. AlSaadi, M.A. Hashim, Potential applications of deep eutectic solvents in nanotechnology, Chem. Eng. J. 273 (2015) 551–567.

[26] R. Svigelj, N. Dossi, C. Grazioli, R. Toniolo, Deep Eutectic Solvents (DESs) and their application in biosensor development, Sensors 21 (2021) 4263.

[27] J.S. Lee, Deep eutectic solvents as versatile media for the synthesis of noble metal nanomaterials, Nanotechnol. Rev. 6 (2017) 271–278.

[28] L. Adhikari, N.E. Larm, G.A. Baker, Batch and Flow nanomanufacturing of large quantities of colloidal silver and gold nanocrystals using Deep Eutectic Solvents, ACS Sustain. Chem. Eng. 8 (39) (2020) 14679–14689.

[29] B.o. Yang, S. Zhang, J. Lv, S. Li, Y. Shi, D. Hu, W. Ma, Large-scale and green production of multi-layer graphene in deep eutectic solvents, J. Mat. Sci. 56 (7) (2021) 4615–4623.

[30] M. Atilhan, S. Aparicio, Molecular dynamics simulations of mixed deep eutectic solvents and their interaction with nanomaterials, J. Mol. Liq. 283 (2019) 147–154.

[31] M.K. AlOmar, M.A. Alsaadi, M. Hayyan, S. Akib, M.A. Hashim, Functionalization of CNTs surface with phosphonium based deep eutectic solvents for arsenic removal from water, Appl. Surf. Sci 389 (2016) 216–226.

[32] Q. Zaib, I. Adeyemi, D.W. Warsinger, I.M. AlNashef, Deep Eutectic Solvent assisted dispersion of carbon nanotubes in water, Front. Chem. 8 (2020) 808.

[33] L. Nie, S. Toufouki, S. Yao, D. Guo, Rethinking the Applications of Ionic Liquids and Deep Eutectic Solvents in Innovative Nano-Sorbents, Front. Chem. 9 (2021).

[34] Y. Shen, F.R. Hung, A molecular simulation study of carbon dioxide uptake by a Deep Eutectic Solvent confined in slit nanopores, J. Phys. Chem. C 121 (44) (2017) 24562–24575.

[35] R.K. Ibrahim, A. El-Shafie, L.S. Hin, N.S.B. Mohd, M.M. Aljumaily, S. Ibraim, M.A. AlSaadi, A clean approach for functionalized carbon nanotubes by deep eutectic solvents and their performance in the adsorption of methyl orange from aqueous solution, J. Environ. Managg. 235 (2019) 521–534.

[36] Y. Liu, J. Xue, X. Zhou, Y. Cui, J. Yin, Deep desulfurization performance of thiophene with deep eutectic solvents loaded carbon nanotube composites, R. Soc. Open Sci. 8 (2021).

[37] Y.K. Fang, M. Osama, W. Rashmi, K. Shahbaz, M. Khalid, F.S. Mjalli, M.M. Farid, Synthesis and thermo-physical properties of deep eutectic solvent-based graphene nanofluids, Nnotecnol. 27 (2016).

[38] D. Fuchs, B.C. Bayer, T. Gupta, G.L. Szabo, R.A. Wilhelm, D. Eder, J.C. Meyer, S. Steiner, B. Gollas, Electrochemical Behavior of Graphene in a Deep Eutectic Solvent, ACS Appl. Mater. Sci. 12 (36) (2020) 40937–40948.

[39] P.J. Bonab, A.R. Ebrahimzadeh, J.J. Sardroodi, Insights into the interactions and dynamics of a DES formed by phenyl propionic acid and choline chloride, Scientific Rep. 11 (2021) 6384.

[40] M. Atilhan, L.T. Costa, S. Aparicio, Elucidating the properties of graphene–Deep Eutectic Solvents interface, Langmuir 33 (2017) 5154–5165.

[41] S. Kaur, S. Sharna, H.K. Kashyap, Bulk and interfacial structures of reline deep eutectic solvent: A molecular dynamics study, J. Chem. Phys. 147 (2017).

[42] M. Shakourian-Fard, S. Maryamdokht, H.R. Ghenaatian, G. Kamath, J.F. Trant, A DFT study of the adsorption of deep eutectic solvents onto graphene and defective graphene nanoflakes, J. Mol. LIQ 327 (2021).

[43] P. Giannozzi, O. Baseggio, P. Bonfà, D. Brunato, R. Car, I. Carnimeo, C. Cavazzoni, S. de Gironcoli, P. Delugas, F. Ferrari Ruffino, A. Ferretti, N. Marzari, I. Timrov, A. Urru, S. Baroni, Quantum ESPRESSO toward the exascale, J. Chem. Phys. 152 (2020) 154105.

[44] A. Jain, S.P. Ong, G. Hautier, W. Chen, W.D. Richards, S. Dacek, S. Cholia, D. Gunter, D. Skinner, G. Ceder, K.A. Persson, The Materials Project: A materials genome approach to accelerating materials innovation, APL Materials 1 (2013).

[45] S. Grimme, A consistent and accurate ab initio parametrization of density functional dispersion correction (DFT-D) for the 94 elements H-Pu, J. Chem. Phys. 132 (2010).

[46] The following pseudopotentials were used: H.pbe-rrkjus_psl.1.0.0.UPF ; O.pbe-rrkjus_psl.1.0.0.UPF;

[47] F.R. Pantano, E.P.M. Leiva, M.I. Rojas, Changes in electronic structure of graphene by adsorption of low melamine coverages, Surf. Sci. 723 (2022).

[48] H.J. Monkhorst, J.D. Pack, Special points for brillouin-zone integrations, Phys. Rev. B 13 (1976) 5188.

[49] A.P. Lyubartsev, A. Laaksonen, MdynaMix – A scalable portable parallel MD simulation package for arbitrary molecular mixtures, Comput. Phys. Commun. 128 (3) (2000) 565–589.

[50] L. Martínez, R. Andrade, E.G. Birgin, J.M. Martínez, Packmol: A package for building initial configurations for molecular dynamics simulations, J. Comput. Chem. 30 (2009) 2157–2164.

[51] W.G. Hoover, Canonical dynamics: Equilibrium phase-space distributions, Phys. Rev. A 31 (1985) 1695.

[52] U. Essmann, L. Perera, M.L. Berkowitz, T. Darden, H. Lee, L.G. Pedersen, A smooth particle mesh ewald method, J. Chem. Phys. 103 (19) (1995) 8577–8593.

[53] W. Humphrey, A. Dalke, K. Schulten, VMD - Visual Molecular Dynamics, J. Molec. Graphics 14 (1) (1996) 33–38.

[54] M. Brehm, B. KirchneR, TRAVIS - A free analyzer and visualizer for Monte Carlo and Molecular Dynamics trajectories, J. Chem. Inf. Model. 51 (2011) 2007–2023.

[55] M. Brehm, H. Weber, M. Thomas, P. Holloczki, B. Kirchner, Domain analysis in nanostructured liquids: a post-molecular dynamics study at the example of ionic liquids, ChemPhysChem 16 (2015) 3271–3277.